

In Vivo Self-Powered Wireless Cardiac Monitoring via Implantable Triboelectric Nanogenerator

Qiang Zheng,^{†,‡} Hao Zhang,^{†,‡} Bojing Shi,^{†,‡} Xiang Xue,[‡] Zhuo Liu,[§] Yiming Jin,[†] Ye Ma,[‡] Yang Zou,[§] Xinxin Wang,[†] Zhao An,[‡] Wei Tang,[†] Wei Zhang,[‡] Fan Yang,[‡] Yang Liu,[‡] Xilong Lang,[‡] Zhiyun Xu,^{*,‡} Zhou Li,^{*,†} and Zhong Lin Wang^{*,†,||}

[†]Beijing Institute of Nanoenergy and Nanosystems, Chinese Academy of Sciences, National Center for Nanoscience and Technology (NCNST), Beijing 100083, China

[‡]Institute of Cardiothoracic Surgery at Changhai Hospital, Second Military Medical University, Shanghai 200433, China

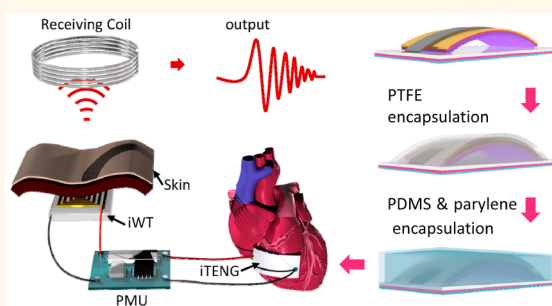
[§]School of Biological Science and Medical Engineering, Beihang University, Beijing 100191, China

^{||}School of Materials Science and Engineering, Georgia Institute of Technology, Atlanta, Georgia 30332-0245, United States

Supporting Information

ABSTRACT: Harvesting biomechanical energy *in vivo* is an important route in obtaining sustainable electric energy for powering implantable medical devices. Here, we demonstrate an innovative implantable triboelectric nanogenerator (iTENG) for *in vivo* biomechanical energy harvesting. Driven by the heartbeat of adult swine, the output voltage and the corresponding current were improved by factors of 3.5 and 25, respectively, compared with the reported *in vivo* output performance of biomechanical energy conversion devices. In addition, the *in vivo* evaluation of the iTENG was demonstrated for over 72 h of implantation, during which the iTENG generated electricity continuously in the active animal. Due to its excellent *in vivo* performance, a self-powered wireless transmission system was fabricated for real-time wireless cardiac monitoring. Given its outstanding *in vivo* output and stability, iTENG can be applied not only to power implantable medical devices but also possibly to fabricate a self-powered, wireless healthcare monitoring system.

KEYWORDS: implantable triboelectric nanogenerator, self-powered, wireless, cardiac monitoring



Implantable electronic devices/systems are crucial medical technologies for monitoring, measuring, and soliciting physiological responses *in vivo*. Over the past decade, the increased *in vivo* stability, miniaturization, and lower energy requirement of electronics have hugely promoted the applications of physiological signal sensors, intelligent gastric and cardiac pacemakers, cochlear implants, and deep brain stimulators;^{1,2} millions of people rely on such implantable medical devices for improved quality of life.^{3,4} However, one of the key challenges for *in vivo* devices is the battery-based power supply,^{5–8} which has limited energy density, short lifetime, chemical side effects, and a large volume. A surgery is unavoidable for replacing the power source, which may cause suffering, risk, and high cost.

Currently, to increase the lifetime and further miniaturization of implantable medical devices, harvesting energy from the human body is a feasible approach for sustainable driving of micro/nanosystems.^{9–13} Piezoelectric (PENG) and triboelectric nanogenerators (TENG), as a potential route for

mechanical-to-electrical energy transduction, have been fabricated recently and shown numerous advantages,^{14–26} but the *in vivo* power output, reliability, and biocompatibility of these energy-harvesting devices are still inadequate for applications in implantable medical systems.^{27,28}

Here, we demonstrate an implantable TENG (iTENG) for *in vivo* biomechanical energy harvesting, which has a multilayered structure and exhibits outstanding *in vivo* performance and stability. Driven by the heartbeat of an adult Yorkshire porcine, the open-circuit voltage (V_{oc}) can reach up to 14 V, and the corresponding short-circuit current (I_{sc}) can be as high as 5 μ A, which were improved by factors of 3.5 and 25, respectively, compared with the reported *in vivo* output performance of biomechanical energy conversion devices based on the piezoelectric or triboelectric effect.^{19,21} In addition, the *in vivo*

Received: April 22, 2016

Accepted: June 2, 2016

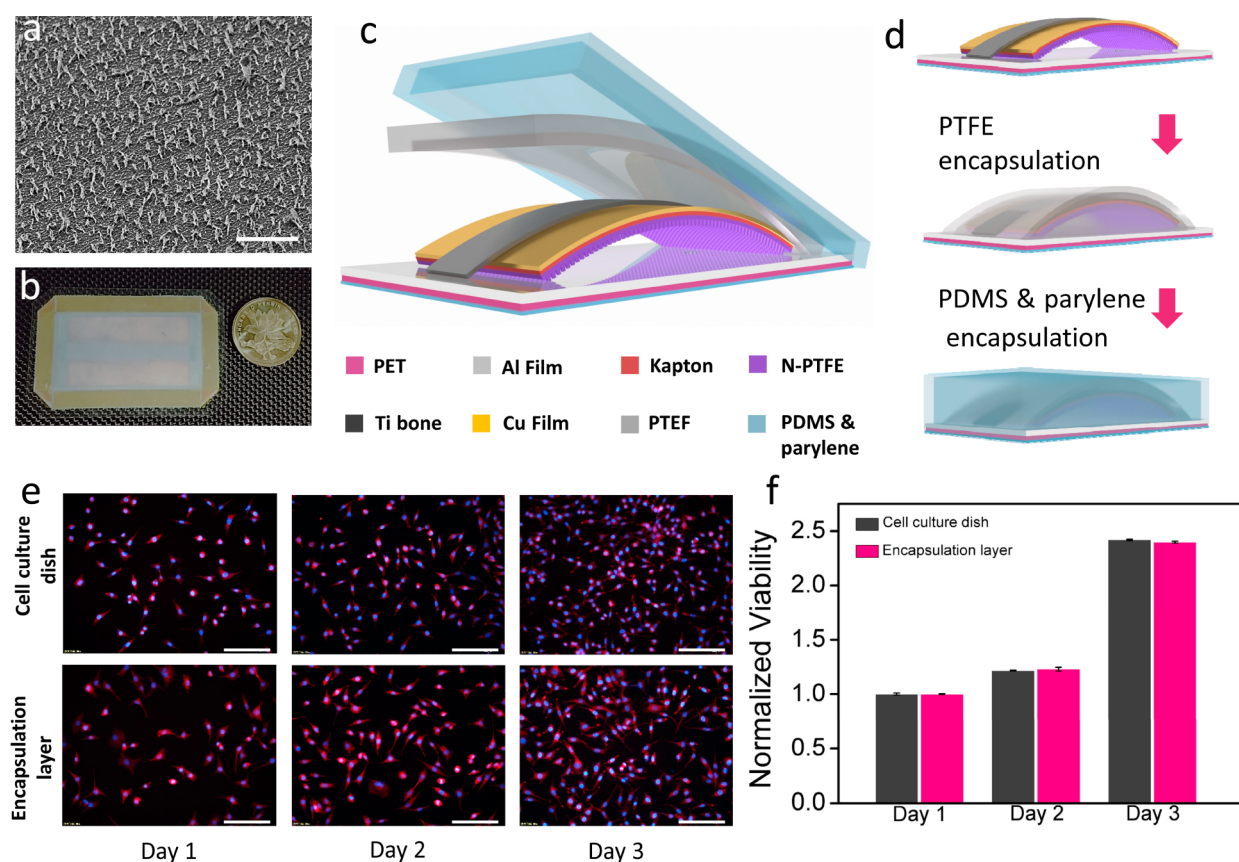


Figure 1. Device structure, surface modification, and cytocompatibility of the iTENG. (a) Scanning electron microscopy image of a nanostructure on the PTFE film (scale bar: 5 μm). (b,c) Schematic diagram and photograph of the iTENG. (d) Encapsulation process of the iTENG. (e) Fluorescence images of stained L929 cells that were cultured on encapsulation layers (scale bar: 100 μm). (f) Cell viability after being cultured for 3 days.

performance of the iTENG was evaluated for over 72 h of implantation, during which the iTENG generated electricity continuously in the active animal. Due to its excellent *in vivo* performance, a self-powered wireless transmission system (SWTS) was fabricated and the electrical signal associated with the *in vivo* heartbeat was successfully transmitted, showing its feasibility for real-time remote cardiac monitoring. Our work demonstrates significant progress for iTENG as a power source for implantable medical devices and its great potential for fabricating a self-powered, wireless healthcare monitoring system.

RESULTS AND DISCUSSION

Device Structure and Encapsulation Strategy. To achieve more ideal leak-proof and output performance *in vivo*, a redesigned structure was introduced for fabricating the iTENG. It was composed of a multilayered structure: core/shell/shell package, “keel structure”, electrode layers, and triboelectric layers (Figure 1b,c). Nanostructured polytetrafluoroethylene (n-PTFE, 50 μm) was employed as the triboelectric layer to increase the output signals (Figure 1a). A Kapton film (150 μm) was fixed on the n-PTFE layer, which served as a flexible substrate. An ultrathin Au layer (50 nm) was deposited on the back of the Kapton film to form one electrode. Al foil (100 μm) served as both another triboelectric layer and the other electrode.

In addition, the effective contact and separation process of the iTENG *in vivo* is one of the challenges for receiving high

output electricity when implanted. A highly resilient titanium strip was introduced as the keel structure of this iTENG. This keel structure significantly strengthened the mechanical property of the overall structure and effectively guaranteed the contact and separation process of the iTENG *in vivo*.

A core/shell/shell package was then applied for device encapsulation. As shown in Figure 1d, PTFE film (50 μm) was used as the core package layer that was proven to exhibit excellent biocompatibility and corrosion resistance for medical devices.²⁹ A flexible polydimethylsiloxane (PDMS) layer (200 μm) covered the entire device as the shell package by spin-coating to enhance the leak-proof performance and the structural stability of the entire device. To further increase the *in vivo* reliability of the iTENG and to avoid potential erosion and adhesion in the physiological environment, parylene C was deposited onto the surface as another shell structure of the device to form a high-density and hole-free coating layer. This “layer by layer” encapsulation strategy can ensure the structural stability of iTENG and its resistance to a complex external environment.

In addition to the hermetization to ensure *in vivo* integrity and reliability of the device under the electrolyte-rich condition, an absence of cytotoxicity is required for the encapsulation layers. Therefore, adherence, growth, and viability of mouse fibroblasts (L929), as a most common tissue cell, were measured on the culture dish and encapsulation material. As a result for both groups, the L929 cells adhered to the encapsulation material as described above, with evident

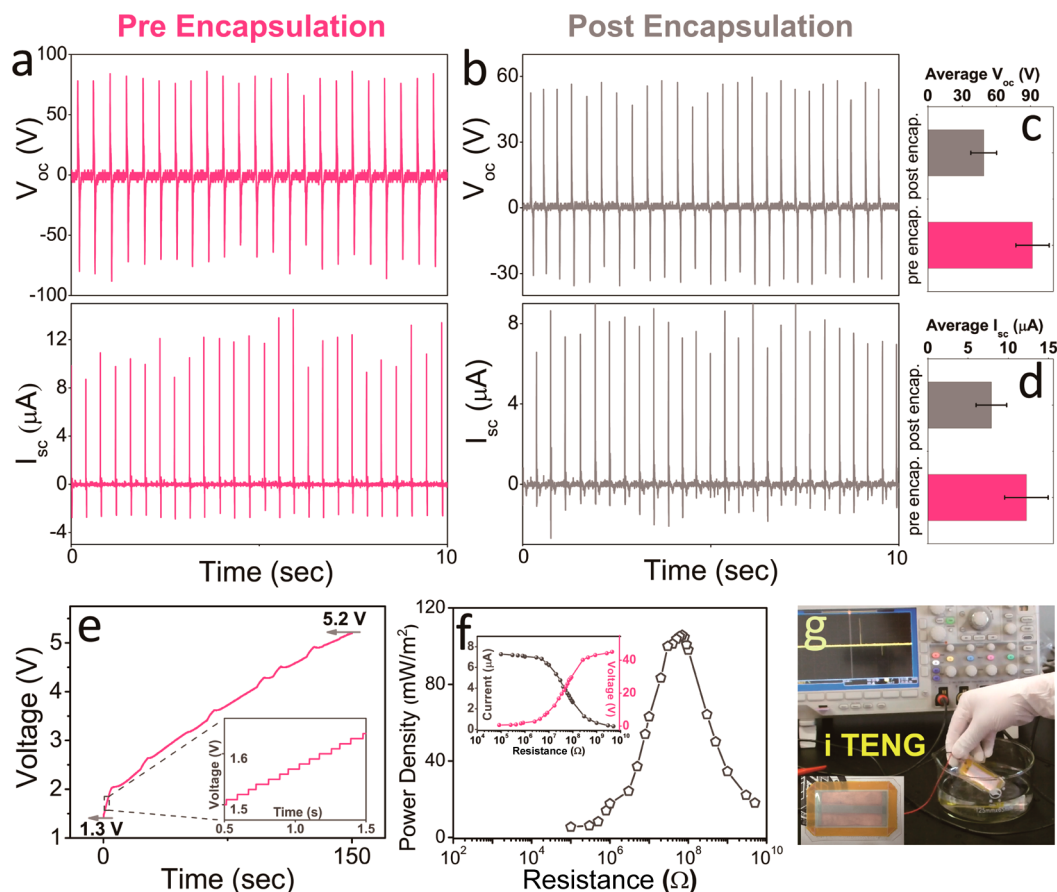


Figure 2. Typical *in vitro* output performance of iTENG. (a) Open-circuit voltage and short-circuit current of the iTENG before encapsulation. (b) Open-circuit voltage and short-circuit current of the iTENG after encapsulation. (c,d) Statistical comparisons of average V_{oc} and I_{sc} of the iTENG before and after encapsulation. (e) Charging curve of a $10\ \mu\text{F}$ capacitor by driving the iTENG with a cyclic tapping in PBS solution (inset: large view of the plotted region, revealing the stepwise behavior of charging). (f) Power density at different load resistances (inset: voltage and current at different load resistances). (g) Photograph of the iTENG when applied in PBS solution.

spreading and intact cytoarchitecture (Figure 1e and Supporting Information Figure S1). Over 98% of the cells were viable after 3 days of culture with no difference between the two groups (Figure 1f).

Electricity-Generating Process and *In Vitro* Output.

The electricity-generating process relies on the relative contact separation between two triboelectric layers, in which a unique coupling between triboelectrification and electrostatic induction gives rise to an alternating flow of electrons between electrodes. This process is described as the vertical contact separation mode of the TENG.^{30,31}

The *in vitro* electrical output of the iTENG was tested before and after encapsulation by applying a periodic external mechanical force. Ten iTENGs with a unified specification were utilized in this experiment. Before encapsulation, the V_{oc} can reach $\sim 90\ \text{V}$ and the I_{sc} can be as high as $\sim 12\ \mu\text{A}$ (Figure 2a). After being encapsulated in the core/shell/shell packages, the iTENG was placed in phosphate-buffered saline (PBS) to test both the output signals and the stability in a physiological solution environment (Figure 2g). A considerable output performance was recorded when tested in PBS solution. The average values of V_{oc} and I_{sc} were $45\ \text{V}$ and $7.5\ \mu\text{A}$, respectively (Figure 2b–d). Resistors were connected as external loads to further investigate the effective electric power of the iTENG when applied in a solution environment. As demonstrated in Figure 2f, the instantaneous current drops with increasing load

resistance due to ohmic loss, while the voltage builds up. Consequently, at a load resistance of $10\ \text{M}\Omega$, a power density of $107\ \text{mW}/\text{m}^2$ for the iTENG was achieved. The iTENG was then connected to a $10\ \mu\text{F}$ capacitor through a rectifier. Within 150 s, the capacitor can be charged from 1.3 to 5.2 V (Figure 2e).

***In Vivo* Electrical Output Performance.** In this study, a large animal model (male adult Yorkshire porcine, 30 kg) was applied to investigate the *in vivo* function of the iTENG. Briefly, after the animal fasted for 12 h prior to surgery, the animal was anesthetized with an injection of ketamine (8 mg/kg, IM) followed by propofol (1 mg/kg, IV) and then was intratracheally intubated and ventilated. Anesthesia was maintained with 1.0% isoflurane. An arterial pressure catheter was placed in the right femoral artery and connected to the data acquisition (DAQ) system through the transducer mentioned above. The surface electrocardiogram (ECG) was also connected to the DAQ system.

The iTENG was set between the heart and pericardium, with the Kapton side facing the inferior wall of the left ventricle (Figure 3a). A periodical contraction and relaxation of the heart actuated the friction layers of the iTENG and resulted in the contact and separation action. An impressive electrical output was recorded through our experiment. Typically, the *in vivo* V_{oc} was up to $\sim 14\ \text{V}$, and the corresponding I_{sc} was $\sim 5\ \mu\text{A}$. As shown in Figure 3d, these electrical signals were synchronized

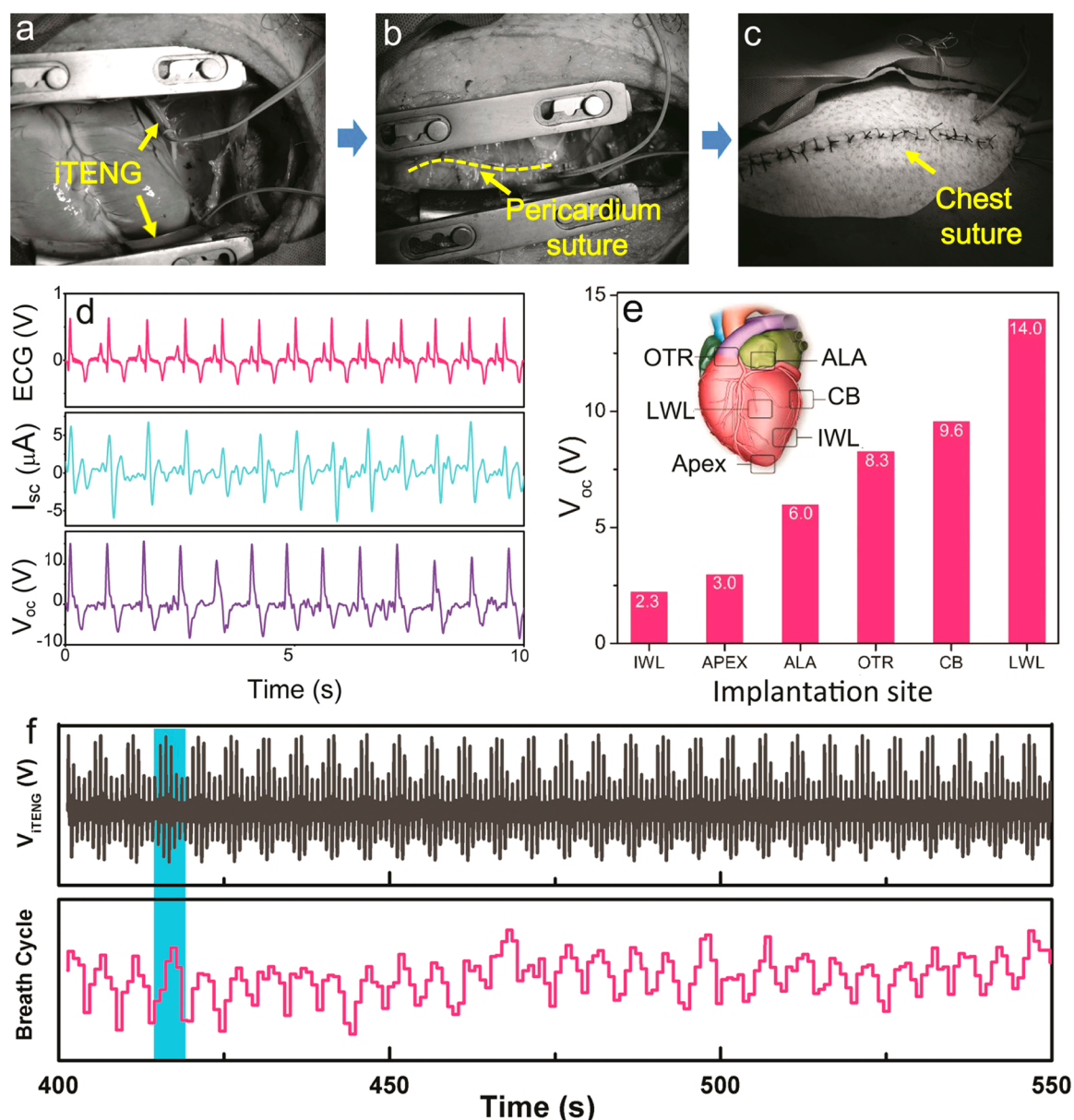


Figure 3. *In vivo* output performance of the iTENG. (a–c) Implantation process of the iTENG: (a) two iTENGs implanted between the heart and the pericardium of swine; (b) pericardium suture; (c) chest and skin suture. (d) *In vivo* V_{oc} and I_{sc} of the iTENG and simultaneously recorded ECG of the swine. (e) Output of the iTENG at a different implant site (OTR, the right ventricular; ALA, the auricle of the left atrium; CB, the cardiac base; LWL, the lateral wall of the left ventricular; IWL, the inferior wall of the left ventricular). (f) Output peaks of the iTENGs presented clear and stable periodical fluctuation, which were consistent with the breath cycle (blue box).

well with the heart rate, revealing that our iTENG was originally driven by the heartbeat motion (Supporting Information Video S1). At a heart rate of 80 bpm, a 1 μF capacitor was charged from 0.2 to 2.8 V beat by beat within 200 s by the iTENG (Supporting Information Figure S4a).

Evaluation of various implantation sites can identify locations for optimal energy harvesting. Analysis of voltage outputs from devices placed on the outflow tract of the right ventricular, the auricle of the left atrium, the cardiac base, the lateral wall of the left ventricular, the inferior wall of the left ventricular, and the apex is shown in Figure 3e. The lateral wall of the left ventricular yields the best output performance (14 V) because the largest motion amplitude and volume of the interspace were achieved in this implantation site.

Several important physiological factors may significantly affect the output performance of the iTENG. In our experiments, respiratory movement can obviously affect the electrical-generating process. The amplitude of electrical output exhibited cyclical changes, as shown in Figure 3, which was synchronized with the breath cycle. In the respiratory process, the movement of the thorax and diaphragm leads to a slight deformation of pericardial cavity. With the deformation of pericardial cavity, the implantation space of the iTENG was compressed and distended periodically, which caused a subsequent periodical change of the electrical output, as shown in Figure 3f.

We also investigated the influence of the cardiac contraction and the heart rate to the iTENG output. As we know, epinephrine can enhance cardiac contractility of the heart,

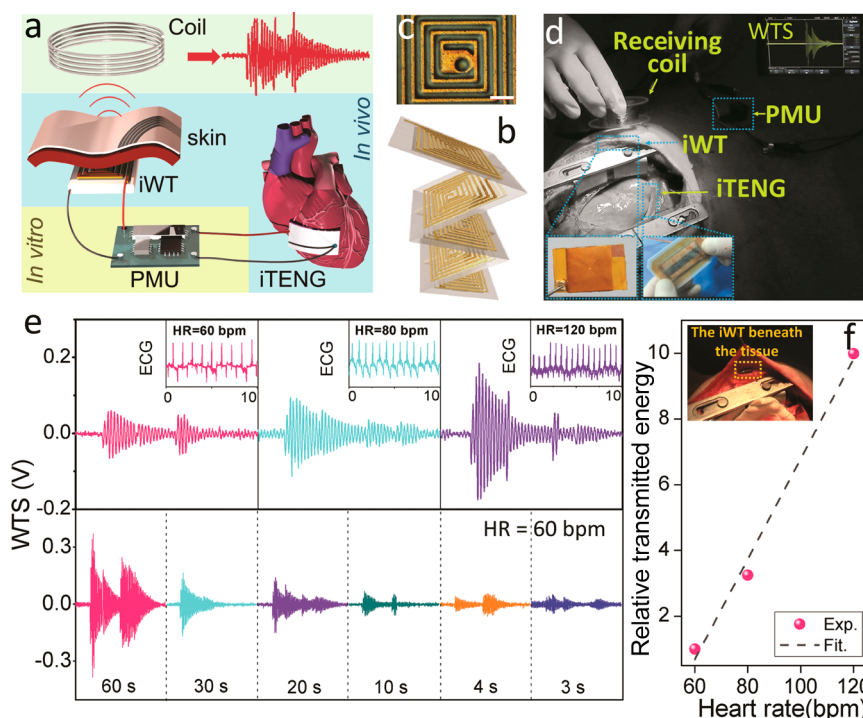


Figure 4. Wireless heart rate monitoring based on the iTENG. (a) Schematic diagram of the self-powered wireless transmission system based on the iTENG (iWT, implantable wireless transmitter; PMU, power management unit; WTS, wireless transmission signal). (b,c) Photograph of the implantable wireless transmitter: (b) schematic diagram of unfolded implantable wireless transmitter, exhibiting the multilayer structure; (c) optical microscope image of an implantable wireless transmitter (scale bar: 50 μm). (d) *In vivo* heart rate monitoring (inset: enlarged view of implantable wireless transmitter, iTENG, and wireless transmission signal). (e) Top: wireless transmission signal as received at different heart rates (charging time = 10 s). Bottom: wireless transmission signal as received at different charging times (HR = 60 bpm). (f) Linear relationship between the heart rate and the normalized wireless transmission signal (inset: implantable wireless transmitter that was implanted under the skin).

which can be represented by the increase of systolic blood pressure. With the injection of epinephrine (0.1 mg/mL, IV), the systolic blood pressure of the tested animal increased from 105 to 250 mmHg, and the as-generated output voltage of the iTENG was synchronously increased by a factor of 3, approximately from 2 to 6 V (Supporting Information Figure S2). This phenomenon demonstrated that the strengthened heart contraction can impact the iTENG more powerfully and thus higher output could be obtained. A heart-rate-related test was performed with the aid of an electronic pacemaker. We modulated the heart rate from 60 to 120 bpm, while no obvious change of the electrical output was detected (Supporting Information Figure S3). This result was consistent with the previous *in vitro* study where the frequency change of an applied force on the TENG at a relatively low range does not significantly affect its electrical output.³⁰

Wireless Electrical Signal Transmission. Wireless transmission is essential for real-time and constant monitoring of physiological signals, which is of great importance for timely diagnosis and treatment of some severe or chronic diseases. Here, we fabricated a SWTS, by which the heartbeat-related electrical energy harvested by the iTENG could be wirelessly delivered to external devices and revealed some real-time cardiac information. A capacitor in a power management unit was charged by the heartbeat-related electrical energy, transmitted through the implantable wireless transmitter, and received by the external receiving coil as electromagnetic waves. The wireless transmitted signal was subsequently recorded with an oscilloscope for further data analysis (Figure

4a,e). The amplitude of the wireless transmitted signal was mainly determined by the total electrical energy stored in the power management unit, which is directly affected by the charging time and the frequency of the applied force. To investigate the potential application of the SWTS as a motion frequency sensor (Supporting Information Figure S6), we fixed the charging time to 10 s; a linear relationship ($R^2 = 0.998$) was established *in vitro* between the frequency of the applied force (0.5–3 Hz), and the wireless transmitted power was represented as the relative transmitted energy (W_R):

$$W_R = \frac{W_n}{W_0} = \left(\frac{\int \varepsilon_n dt}{\int \varepsilon_0 dt} \right)^2 \quad (1)$$

where ε is the induced electromotive force of the receiving coil recorded by oscilloscope; W_n is the wireless transmitted power at a certain frequency of the applied force ($n = 0.5, 1, 1.5, 2, 2.5,$ and 3); W_0 is the wireless transmitted power at a frequency of 0.5 Hz.

Through this simple signal processing, we can directly interpret the frequency from the recorded wireless transmitted signal (Supporting Information Figure S4b–d and Video S2). Based on these results, we applied the SWTS for *in vivo* heart rate monitoring (Figure 4a,d and Video S3). As shown in Figure 4, the different heart rates (60, 80, and 120 bpm) modulated by the electronic pacemaker were successfully monitored by the SWTS ($R^2 = 0.983$); the results were consistent with the simultaneously recorded ECG signal (Figure 4f). Moreover, by charging for only 3 s at the heart

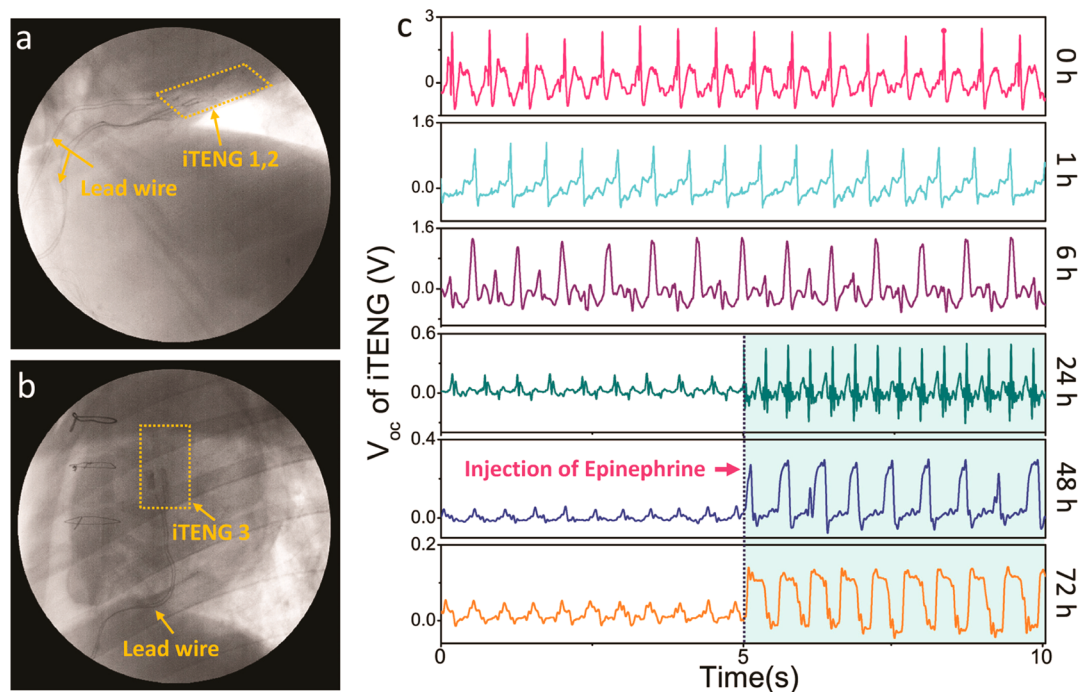


Figure 5. Long-term evaluation of the iTENG *in vivo*. (a,b) Real-time *in vivo* monitoring of the iTENG by digital radiography imaging. The yellow plotted regions show the locations of the implanted iTENG. (c) *In vivo* output performance of the iTENG over 72 h.

rate of 60 bpm, the stored energy in the power management unit was sufficient to transmit wireless data, showing the outstanding sensitivity of the SWTS (Figure 4e and Supporting Information Figure S5a–c).

Long-Term Service Evaluation. The peri-implant space is a chemically harsh environment, in which the highly conductive and corrosive physiological medium carrying various reactive biochemical molecules will continuously attack the surface of the implant. Mechanical motion from the surrounding organs will also influence the implanted device and undermine the robustness. Therefore, long-term implantation is still challenging for *in vivo* energy-harvesting devices. Here, in an effort to estimate the long-term *in vivo* reliability, three iTENGs were implanted in two swine. The iTENGs were fixed on the pericardium by suture, with iTENG 1 and iTENG 2 facing the sites on the left ventricle and the right ventricle of swine 1, respectively. The iTENG 3 faced the cardiac base of swine 2. The anchoring scheme used suture at four points to minimize any alternation or constraint on the cardiac motion. No detectable change in cardiac constriction or epicardial motion occurred following this procedure for fixing the device.

The electrical signals were detected and recorded at different time intervals to estimate the function of the iTENG *in vivo*, immediately following the implantation, the suture, and the post-anesthetic recovery. As shown in Figure 5, electrical signals can be detected, revealing that the iTENG maintained its function during the period of 72 h. After 24 h of implantation, the voltage exhibited an obvious decrease compared with the initial output. This reduction could be attributed to the weakened cardiac function that might be related to surgery because the output of the iTENG was significantly increased when the epinephrine was administered.

The *in vivo* working state of the iTENG and cardiac motion was further observed by digital radiography (Supporting Information Video S4). Throughout the test, iTENGs maintained their position and showed an inconspicuous effect

on cardiac motion. Furthermore, the histology study of the myocardium from the implantation site showed no detectable inflammatory reaction, and none of cardiomyocyte was labeled for cleaved/activated caspase 3 or presented the nuclear characteristics of apoptosis, prompting no influence on the body. These results demonstrated a favorable biocompatibility of the device (Supporting Information Figure S5d,e).

The TENG is an efficient mechanical energy-harvesting technology,^{32–36} and it exhibits great potential for powering implantable medical devices.²¹ This potential is crucial for improving the disadvantages of current battery technologies and promoting the emergence of sustainable medical devices. It was known that the output performance of the TENG was heavily affected by the area of friction layers and the scale of implied external force. The size of a previously reported iTENG was significantly restricted in the small animal model. A larger animal model is indispensable for realistically simulating the human implantation environment and permitting a larger iTENG size, although the difficulty of surgery and post-operative care will increase significantly. We chose a male Yorkshire porcine (30 kg) as the animal model because it is widely used in surgical experiments. The implant site was also carefully evaluated because it directly contributes to the scale of the implied force on the iTENG and the peri-implant environment (Figure 3e). In our work, the iTENG was set between the heart and pericardium by fixing it on the inner side of the pericardium because the heart is one of the most powerful organs inside our body, which can effectively drive the iTENG. Moreover, the space between the heart and pericardium is fairly sufficient for accommodating the iTENG, in which the iTENG will not affect the normal heart motion and give rise to any obvious discomfort, which was further confirmed by the digital radiography imaging and post-operative monitoring.

Actually, the contact and separation process of the iTENG relied on the mechanical resilience of the Kapton substrate.

While, for *in vivo* application, both the narrow space of the implantation site and the encapsulation structure increased the burden of the Kapton substrate to recover from its deformation when an external mechanical load was released. Therefore, we integrated a keel structure of a Ti strip with the Kapton substrate to strengthen the mechanical properties of the iTENG. This structure can offset the above-mentioned “burden” as much as possible and effectively guarantee the contact and separation process of the iTENG *in vivo*.

Long-term reliability is another crucial factor for implantation in a living body, which is very dependent on the encapsulation strategy. The encapsulation layers have two roles. For one, the hermetic packaging ensures the *in vivo* electronic performance of the devices and protects the iTENG over the lifetime under specific physiological conditions. Here, to offer both reliability and flexibility, the iTENG was packaged by soft materials layer by layer, forming a robust core/shell/shell structure. The iTENG exhibited a good leakproofness for both *in vitro* and *in vivo* tests. Second, the encapsulation layer plays an important role for protecting the host tissues from potentially toxic elements of the device. Thus, the biocompatibility and biodegradation properties of the materials should be carefully considered. The selected encapsulation materials in this work were proven to be biocompatible and resistant to a chemically harsh environment.²⁹

CONCLUSION

In summary, this design of the iTENG enables high output performance and robust operation *in vivo*. The *in vivo* output voltage reached up to 14 V, enhanced by a factor of 3.5, and the corresponding output current was increased to 5 μA , enhanced by a factor of 25 compared to the previously reported *in vivo* output performance of biomechanical energy conversion devices.^{19,21} The long-term reliability of the iTENG was also significantly improved, thereby providing a promising power source for implantable medical devices. Because our device can directly indicate the physiological heartbeating behavior, a self-powered wireless data transmission system was fabricated for real-time remote cardiac monitoring by connecting it with an implantable wireless transmitter. With a simple data process, the real-time heartbeat of an adult Yorkshire porcine was successfully monitored through the wireless transmitted signal, showing the potential for fabricating a self-powered, wireless healthcare monitoring system.

EXPERIMENTAL SECTION

Cell Biocompatibility. *Cell Culture.* The L929 cells were purchased from Central South University (Hunan, China). The cells were cultured in a 75 cm^2 flask with RPMI medium 1640 basic (1 \times), supplemented with 10% fetal bovine serum (Gibco) and 1% penicillin–streptomycin solution (Life Technologies, Shanghai, China) at 37 $^\circ\text{C}$ in a humidified atmosphere with 5% CO_2 .

Cell Viability. After being cultured for 3 days, L929 cells were seeded in 24-well plates. Trypan blue staining showed that 85.6% of L929 cells were positive. The cells of the experimental group were exposed to the parylene (parylene C, PALS Ltd.)-coated PDMS (SYLGARD 184, Dow Corning) film on the 24-well plates. The proliferation of the cultured L929 cells was determined using the MTT (3-(4,5-dimethylthiazol-2-yl)-2,5-diphenyl-2H-tetrazolium bromide) assay. In particular, the culture medium was removed, and 100 μL of MTT solution was added to each well. Upon incubation at 37 $^\circ\text{C}$ for 4 h in a humidified atmosphere with 5% CO_2 , MTT was taken up by active cells and reduced in the mitochondria to insoluble purple formazan granules; subsequently, the medium was discarded, the

precipitated formazan was dissolved in DMSO (600 μL /well), and then the optical density of the solution was evaluated using a microplate spectrophotometer at a wavelength of 490 nm. The analytical assays were performed at day 1, day 2, and day 3. At least three wells were randomly examined each time.

Cell Morphology and Immunofluorescent Staining. The cytoskeleton and nucleus were stained with phalloidin and DAPI, respectively. The samples were fixed with immunohistochemically fixed fluid (Beyotime) for 30 min and then rinsed three times with prewarmed PBS. The samples were blocked with 0.1% bovine serum albumin solution for 1 h at 37 $^\circ\text{C}$ and then incubated with DAPI (1:400 dilution) and Alexa Fluor phalloidin 568 conjugate (1:200 dilution) for 2 h at 37 $^\circ\text{C}$. L929 cells were imaged using an inversion fluorescence microscope.

In Vivo Study. The animal was handled in accordance with the IACUC approval protocol of the Animal Care Center at the Second Military Medical University. The male Yorkshire porcine (30 kg) fasted for 12 h prior to surgery. Briefly, the animal was anesthetized with an injection of ketamine (8 mg/kg, IM), followed by propofol (1 mg/kg, IV), and then intratracheally intubated and ventilated. Anesthesia was maintained with 1.0% isoflurane. An arterial pressure catheter was placed in the right femoral artery and connected to the DAQ system through the transducer mentioned above. The surface ECG was also connected to the DAQ system.

Next, the iTENG was implanted and fixed to the pericardium facing the inferior wall of the left ventricle with a 4–0 prolene suture. The electrodes of the iTENG were connected to the DAQ system to measure the electric output.

Epinephrine (0.1 mg/mL, IV) was administered as the α -receptor agonist to increase the heart rate to simulate the status of tachycardia. Esmolol hydrochloride (0.1 mg/mL, IV) was used as the β -receptor blocker to decrease the heart rate to imitate the status of bradycardia. Two pacing leads were sutured into the epicardium of the left ventricle and then connected to an electronic cardiac pacemaker (St. Jude Medical, USA), which can be set to the range of 50–120 beats per minute in enforce mode to modulate the frequent ventricular premature contractions.

Wireless Transmission Experiments. The wireless transmission system consisted of three parts: the iTENG, the power management unit, and the signal transmission unit (Supporting Information Figure S5). The indwelling component of the signal transmission unit was an implantable wireless transmitter (iWT), which was implanted into a subcutaneous sac 5 mm under the epidermis and transmitted the electrical signals. Next, the signal was received by the external component of the signal transmission unit (receiving coil). To fabricate the iWT, a multilayer structure (five layers) was used to increase the transmission efficiency. Cu wires were fabricated on both surfaces of each thin Kapton layer (thickness was 90 μm) by printing circuit technology (Figure 4c). The line width of the coil was 100 μm (Figure 4b). The number of turns on each layer was 46, so the total number was 230. PDMS was used to package iWT, and the overall size was approximately 25 mm \times 10 mm \times 1.5 mm. The receiving coil was *in vitro* to receive signals from the implanted coil. The diameter of the Cu wire was 0.1 mm and tangled on a cylinder. The number of turns was 1000; the diameter of the coil was approximately 4 cm, and the height was approximately 2 cm.

The iTENG was connected to the power management unit, which consists of a rectifier (DB107, SEP Electronic Corp.), a capacitor (1 μF , Risym), and a switch (R19A, Light Country Corp.). When the switch was turned on, the electricity generated by the TENG was stored in the capacitor through a rectifier. Next, when switched off, electric energy was emitted through the iWT and received by the receiving coil in the form of electromagnetic waves. Simultaneously, the electromagnetic signals were captured by the receiving coil and displayed on the oscilloscope.

The TENG was driven by the line motor under different frequency conditions as 0.5, 1, 1.5, 2, 2.5, and 3 Hz. The testing time was 10 s.

$$\epsilon = -M \frac{di}{dt} \quad (2)$$

where ε is the induced electromotive force of the receiving coil captured by oscilloscope; M is mutual inductance coefficient; i is the current in the launch coil. Therefore

$$\int \varepsilon dt \propto i \quad (3)$$

The energy (W) can be given by

$$W = i^2 R t \quad (4)$$

Here, R is the resistance of the receiving coil and t is the testing time. Because the device and testing time were the same, we obtain

$$W \propto i^2 \propto \left(\int \varepsilon dt \right)^2 \quad (5)$$

In eq 1, we used W_n/W_0 as the relative energy to evaluate the energy of the receiving coil. We set the time integral of the induced electromotive force generated on the receiving coil under the condition of the TENG driven by the linear motor at 0.5 Hz expressed by $(\int \varepsilon_{0.5} dt)^2$ as the energy benchmark " W_0 ". Therefore, the other energy of the receiving coil was the ratio of $(\int \varepsilon_{0.5} dt)^2$.

ASSOCIATED CONTENT

Supporting Information

The Supporting Information is available free of charge on the ACS Publications website at DOI: 10.1021/acsnano.6b02693.

Detailed data and images (PDF)

Video S1 (AVI)

Video S2 (AVI)

Video S3 (AVI)

Video S4 (AVI)

AUTHOR INFORMATION

Corresponding Authors

*E-mail: zhiyunx@hotmail.com.

*E-mail: zli@binn.cas.cn.

*E-mail: zlwang@binn.cas.cn.

Author Contributions

[†]Q.Z., H.Z., and B.S. contributed equally to this work.

Notes

The authors declare no competing financial interest.

ACKNOWLEDGMENTS

This work was supported by the "Thousands Talents" program for pioneer researcher and his innovation team, NSFC 31571006 and Beijing Talents Fund (2015000021223ZK21).

REFERENCES

- (1) Majerus, S. J. A.; Garverick, S. L.; Suster, M. A.; Fletter, P. C.; Damaser, M. S. Wireless, Ultra-Low-Power Implantable Sensor for Chronic Bladder Pressure Monitoring. *J. Emerg. Technol. Com.* **2012**, *8*, 1.
- (2) Cheng, A.; Tereshchenko, L. G. Evolutionary Innovations in Cardiac Pacing. *J. Electrocardiol* **2011**, *44*, 611–615.
- (3) Halperin, D.; Kohno, T.; Heydt-Benjamin, T. S.; Fu, K.; Maisel, W. H. Security and Privacy for Implantable Medical Devices. *Ieee Pervas. Comput.* **2008**, *7*, 30–39.
- (4) Stellbrink, C.; Trappe, H. J. The Follow-Up of Cardiac Devices: What To Expect for The Future? *Eur. Heart J. Suppl.* **2007**, *9*, I113–I115.
- (5) Ko, W. H. Early History and Challenges of Implantable Electronics. *J. Emerg. Technol. Com.* **2012**, *8*, 1.
- (6) Kennergren, C. Reliability of Cardiac Implantable Electronic Device Leads. *Europace* **2013**, *15*, 165–166.

(7) von Lueder, T. G.; Krum, H. Current Modalities for Invasive and Non-Invasive Monitoring of Volume Status In Heart Failure. *Heart* **2012**, *98*, 967–973.

(8) Bazaka, K.; Jacob, M. Implantable Devices: Issues and Challenges. *Electronics* **2013**, *2*, 1–34.

(9) Rapoport, B. I.; Kedzierski, J. T.; Sarpeshkar, R. A Glucose Fuel Cell for Implantable Brain-Machine Interfaces. *PLoS One* **2012**, *7*, e38436.

(10) Justin, G. A.; Zhang, Y. Z.; Sun, M.; Scلابassi, R. Biofuel Cells: A Possible Power Source for Implantable Electronic Devices. *Proceedings of the 26th Annual International Conference of the IEEE Engineering in Medicine and Biology Society*, San Francisco, CA, 2004; Vols. 1–7, pp 4096–4099.

(11) Occhiuzzi, C.; Contri, G.; Marrocco, G. Design of Implanted RFID Tags for Passive Sensing of Human Body: The STENTag. *IEEE Trans. Antennas Propag.* **2012**, *60*, 3146–3154.

(12) Mercier, P. P.; Lysaght, A. C.; Bandyopadhyay, S.; Chandrakasan, A. P.; Stankovic, K. M. Energy Extraction from The Biologic Battery in The Inner Ear. *Nat. Biotechnol.* **2012**, *30*, 1240–1243.

(13) Halamkova, L.; Halamek, J.; Bocharova, V.; Szczupak, A.; Alfonta, L.; Katz, E. Implanted Biofuel Cell Operating in A Living Snail. *J. Am. Chem. Soc.* **2012**, *134*, 5040–5043.

(14) Wang, Z. L.; Song, J. H. Piezoelectric Nanogenerators Based On Zinc Oxide Nanowire Arrays. *Science* **2006**, *312*, 242–246.

(15) Choi, M. Y.; Choi, D.; Jin, M. J.; Kim, I.; Kim, S. H.; Choi, J. Y.; Lee, S. Y.; Kim, J. M.; Kim, S. W. Mechanically Powered Transparent Flexible Charge-Generating Nanodevices with Piezoelectric ZnO Nanorods. *Adv. Mater.* **2009**, *21*, 2185–2189.

(16) Chen, X.; Xu, S. Y.; Yao, N.; Shi, Y. 1.6 V Nanogenerator for Mechanical Energy Harvesting Using PZT Nanofibers. *Nano Lett.* **2010**, *10*, 2133–2137.

(17) Hwang, G. T.; Park, H.; Lee, J. H.; Oh, S.; Park, K. I.; Byun, M.; Park, H.; Ahn, G.; Jeong, C. K.; No, K.; Kwon, H.; Lee, S. G.; Joung, B.; Lee, K. J. Self-Powered Cardiac Pacemaker Enabled by Flexible Single Crystalline PMN-PT Piezoelectric Energy Harvester. *Adv. Mater.* **2014**, *26*, 4880–4887.

(18) Li, Z.; Zhu, G. A.; Yang, R. S.; Wang, A. C.; Wang, Z. L. Muscle-Driven *In Vivo* Nanogenerator. *Adv. Mater.* **2010**, *22*, 2534–2537.

(19) Dagdeviren, C.; Yang, B. D.; Su, Y. W.; Tran, P. L.; Joe, P.; Anderson, E.; Xia, J.; Doraiswamy, V.; Dehdashti, B.; Feng, X.; Lu, B. W.; Poston, R.; Khalpey, Z.; Ghaffari, R.; Huang, Y. G.; Slepian, M. J.; Rogers, J. A. Conformal Piezoelectric Energy Harvesting and Storage from Motions of The Heart, Lung, and Diaphragm. *Proc. Natl. Acad. Sci. U. S. A.* **2014**, *111*, 1927–1932.

(20) Dagdeviren, C.; Shi, Y.; Joe, P.; Ghaffari, R.; Balooch, G.; Usgaonkar, K.; Gur, O.; Tran, P. L.; Crosby, J. R.; Meyer, M.; Su, Y. W.; Webb, R. C.; Tedesco, A. S.; Slepian, M. J.; Huang, Y. G.; Rogers, J. A. Conformal Piezoelectric Systems for Clinical and Experimental Characterization of Soft Tissue Biomechanics. *Nat. Mater.* **2015**, *14*, 728–736.

(21) Zheng, Q.; Shi, B. J.; Fan, F. R.; Wang, X. X.; Yan, L.; Yuan, W. W.; Wang, S. H.; Liu, H.; Li, Z.; Wang, Z. L. *In Vivo* Powering of Pacemaker by Breathing-Driven Implanted Triboelectric Nanogenerator. *Adv. Mater.* **2014**, *26*, 5851–5856.

(22) Zhang, H.; Zhang, X. S.; Cheng, X. L.; Liu, Y.; Han, M. D.; Xue, X.; Wang, S. F.; Yang, F.; Smitha, A. S.; Zhang, H. X.; Xu, Z. Y. A Flexible And Implantable Piezoelectric Generator Harvesting Energy From The Pulsation of Ascending Aorta: *In Vitro* And *In Vivo* Studies. *Nano Energy* **2015**, *12*, 296–304.

(23) Shi, B.; Zheng, Q.; Jiang, W.; Yan, L.; Wang, X.; Liu, H.; Yao, Y.; Li, Z.; Wang, Z. L. A Packaged Self-Powered System With Universal Connectors Based on Hybridized Nanogenerators. *Adv. Mater.* **2016**, *28*, 846–852.

(24) Cheng, Li.; Yuan, M.; Gu, L.; Wang, Z.; Qin, Y.; Jing, T.; Wang, Z. L. Wireless, Power-Free And Implantable Nanosystem for Resistance-Based Biodetection. *Nano Energy* **2015**, *15*, 598–606.

(25) Yuan, M.; Cheng, L.; Xu, Q.; Wu, W.; Bai, S.; Gu, L.; Wang, Z.; Lu, J.; Li, H.; Qin, Y.; Jing, T.; Wang, Z. L. Biocompatible

Nanogenerators through High Piezoelectric Coefficient 0.5Ba-(Zr_{0.2}Ti_{0.8})O₃-0.5(Ba_{0.7}Ca_{0.3})TiO₃ Nanowires for *In-Vivo* Applications. *Adv. Mater.* **2014**, *26*, 7432–7437.

(26) Zheng, Q.; Zou, Y.; Zhang, Y.; Liu, Z.; Shi, B.; Wang, X.; Jin, Y.; Ouyang, H.; Li, Z.; Wang, Z. L. Biodegradable Triboelectric Nanogenerator as A Life-Time Designed Implantable Power Source. *Sci. Adv.* **2016**, *2*, e1501478.

(27) Paralikar, K.; Cong, P.; Yizhar, O.; Fenno, L. E.; Santa, W.; Nielsen, C.; Dinsmoor, D.; Hocken, B.; Munns, G. O.; Giftakis, J.; Deisseroth, K.; Denison, T. An Implantable Optical Stimulation Delivery System for Actuating an Excitable Biosubstrate. *IEEE J. Solid-State Circuits* **2011**, *46*, 321–332.

(28) Nagpal, A.; Baddour, L. M.; Sohail, M. R. Microbiology and Pathogenesis of Cardiovascular Implantable Electronic Device Infections. *Circ.: Arrhythmia Electrophysiol.* **2012**, *5*, 433–441.

(29) Wang, X. *Overview on Biocompatibilities of Implantable Biomaterials*; INTECH, 2013; p 568.

(30) Fan, F. R.; Tian, Z. Q.; Wang, Z. L. Flexible Triboelectric Generator! *Nano Energy* **2012**, *1*, 328–334.

(31) Wang, Z. L.; Chen, J.; Lin, L. Progress In Triboelectric Nanogenerators as A New Energy Technology And Self-Powered Sensors. *Energy Environ. Sci.* **2015**, *8*, 2250–2282.

(32) Zhu, G.; Lin, Z. H.; Jing, Q. S.; Bai, P.; Pan, C. F.; Yang, Y.; Zhou, Y. S.; Wang, Z. L. Toward Large-Scale Energy Harvesting by A Nanoparticle-Enhanced Triboelectric Nanogenerator. *Nano Lett.* **2013**, *13*, 847–853.

(33) Wang, S. H.; Lin, Z. H.; Niu, S. M.; Lin, L.; Xie, Y. N.; Pradel, K. C.; Wang, Z. L. Motion Charged Battery as Sustainable Flexible-Power-Unit. *ACS Nano* **2013**, *7*, 11263–11271.

(34) Zhang, H. L.; Yang, Y.; Hou, T. C.; Su, Y. J.; Hu, C. G.; Wang, Z. L. Triboelectric Nanogenerator Built Inside Clothes for Self-Powered Glucose Biosensors. *Nano Energy* **2013**, *2*, 1019–1024.

(35) Hou, T. C.; Yang, Y.; Zhang, H. L.; Chen, J.; Chen, L. J.; Wang, Z. L. Triboelectric Nanogenerator Built Inside Shoe Insole For Harvesting Walking Energy. *Nano Energy* **2013**, *2*, 856–862.

(36) Yang, W. Q.; Chen, J.; Zhu, G.; Yang, J.; Bai, P.; Su, Y. J.; Jing, Q. S.; Cao, X.; Wang, Z. L. Harvesting Energy From The Natural Vibration Of Human Walking. *ACS Nano* **2013**, *7*, 11317–11324.